

Evolution of spectral properties along the O(6)-U(5) transition in the interacting boson model. II. Classical trajectories

Michal Macek¹, Pavel Cejnar¹, Jan Jolie², Stefan Heinze²

¹*Faculty of Mathematics and Physics, Charles University,
V Holešovičkách 2, 180 00 Prague, Czech Republic*

²*Institute of Nuclear Physics, University of Cologne, Zùlpicherstrasse 77, 50937 Cologne, Germany*

(Dated: February 9, 2020)

This article continues our previous study of level dynamics in the [O(6)-U(5)] \supset O(5) transition of the interacting boson model [Phys. Rev. C **XX**, xxxxxx (2005)] using the semiclassical theory of spectral fluctuations. We find classical monodromy, related to a singular bundle of orbits with infinite period at energy $E = 0$, and bifurcations of numerous periodic orbits for $E > 0$. The spectrum of allowed ratios of periods associated with β - and γ -vibrations exhibits an abrupt change around zero energy. These findings explain anomalous bunching of quantum states in the $E \approx 0$ region, which is responsible for the redistribution of levels between O(6) and U(5) multiplets.

PACS numbers: 21.60.Ev, 03.65.Sq

I. INTRODUCTION

In the first part of this work [1] (hereafter referred to as Part I), we have discussed the evolution of level energies and wave functions along the [O(6)-U(5)] \supset O(5) transition in the interacting boson model (IBM) [2]. It is known that this transitional class is integrable—due to the O(5) underlying symmetry and the associated seniority quantum number v —and exhibits a second-order ground-state phase transition from deformed γ -soft to spherical equilibrium shapes.

Remind that our family of model Hamiltonians is given by

$$\hat{H}(\eta) = a \left[-\frac{1-\eta}{N^2} (\hat{Q} \cdot \hat{Q}) + \frac{\eta}{N} \hat{n}_d \right], \quad (1)$$

with $\eta \in [0, 1]$ denoting a dimensionless control parameter that drives the system between the O(6) ($\eta = 0$) and U(5) ($\eta = 1$) dynamical symmetries. The spectrum of $\hat{H}(\eta)$ at any point of the transitional path depends on the specific interplay of both terms in Eq. (1), where $\hat{Q} = [s^\dagger \tilde{d} + d^\dagger \tilde{s}]^{(2)}$ represents the quadrupole operator and $\hat{n}_d = (d^\dagger \cdot \tilde{d})$ the d -boson number operator. Note that N is the total number of bosons, which in the classical limit tends to infinity (both terms in the above Hamiltonian are properly normalized by the N^k denominators to yield finite contributions in this limit), and $a = 1$ MeV is an arbitrary scaling factor. The $N \rightarrow \infty$ ground-state shape-phase transitions takes place at $\eta_c = \frac{4}{5}$.

We have shown that one of the most significant features of spectra in the $\eta \in [0, 1]$ transitional regime of Hamiltonian (1) is the pattern of alternating compressions and dilutions of levels with angular momentum $l = 0$ around energy $E \approx 0$. This pattern spreads over a wide interval of the control parameter between $\eta \approx 0.3$ and 0.8, see Fig. 1 in Part I. After deconvoluting spectra with different seniorities, it transforms into a sequence of avoided crossings that constitute what we called the “shock-wave scenario” [1].

The level bunching pattern represents basically a huge oscillation of the level density in the $E \approx 0$ region, not dissimilar to shell effects in single-particle spectra of some quantum-mechanical potentials. There exists a deep and far-reaching relation between fluctuations of the quantum level density and properties of periodic orbits in the classical counterpart of the given system [3, 4]. While it is known that each periodic orbit brings one oscillatory term into the level density, with an amplitude related to the orbit’s dimensionality and stability [5, 6, 7], the interference of several such terms gives rise to spectral *beating patterns* that underlie shell effects in nuclei, quantum dots, or metallic clusters [8]. Indeed, as follows from the analysis performed by Balian and Bloch [6], the inclusion of just two simplest periodic orbits in a spheroidal cavity explains the essentials of the shell structure in these systems.

Majority of semiclassical studies on the level-density fluctuations was performed for hard-wall systems—two-dimensional billiards or three-dimensional cavities [3, 4]. In these systems, the calculation is considerably simplified since each individual orbit exists with easily predictable properties for all energies of the particle bouncing between the walls and contributes by a well-defined term to the single-particle level density. Nevertheless, the influence of periodic orbits is equally important also in systems with “soft” potentials, where the orbit analysis is much more involved. This is also the case of IBM, where the classical limit for $l = 0$ describes two-dimensional motions within a bounded (for each finite E) range of quadrupole deformation parameters, governed by a Hamiltonian containing specific kinetic and potential terms [9, 10, 11, 12].

The purpose of the present part of our contribution is to show that the shell effects and the IBM level bunching phenomenon are indeed of similar nature, both originating in some particular features of classical periodic trajectories. Nevertheless, our reasoning does not only point to ordinary beating patterns, known from hard-wall systems, but makes use of two concepts that in the context

of nuclear models are somewhat less usual. The first one relies on *bifurcations* of periodic orbits [13], the second on *monodromy* in classical and quantum integrable systems [14]. Both these effects lead to singular contributions to semiclassical trace formulas, that provide a simplified description of the level-density fluctuations. Therefore, they can be potentially linked to anomalous effects in quantal spectra, such as the level bunching at $E \approx 0$.

The paper is organized as follows: In Section II we review the construction of the classical limit of the IBM Hamiltonian under study and describe basic features of the resulting classical dynamics. Subsection III A briefly recapitulates the Berry-Tabor trace formula and the role of singular orbits and bifurcations in the semiclassical theory of quantal spectra. Numerical analysis of orbits with $l = 0$, presented in Sec. III B, shows that in the $E \approx 0$ region our system passes through a robust structural change of classical dynamics. This change is correlated with the occurrence of a singular bundle of $E = 0$ trajectories and triggers multiple bifurcations of orbits in the region $E > 0$. The relation of these findings to the concept of monodromy is discussed in Section IV. Finally, Section V contains concluding remarks.

II. CLASSICAL HAMILTONIAN

The classical limit of the IBM can be obtained via the well-known procedure, elaborated in detail by Hatch and Levit [9], and by Alhassid and Whelan [10, 11, 12]. The procedure makes use of Glauber coherent states $|\alpha\rangle \propto \exp(\alpha_s s^\dagger + \sum_\mu \alpha_\mu d_\mu^\dagger)|0\rangle$ with complex time-dependent coefficients $\alpha \equiv \{\alpha_s, \alpha_\mu\}_{\mu=-2, \dots, +2}$ which define a set of 12 classical-like variables (both coordinates and momenta). The equations of motion for α are derived from the time-dependent variational principle, which results in the Hamilton function given by the coherent-state average $H_{\text{cl}}(\eta; \alpha) = \langle \alpha | \hat{H}(\eta) | \alpha \rangle$. This function and analogous counterparts of other operators can be obtained by substitutions $s, d_\mu \mapsto \alpha_s, \alpha_\mu$ and $s^\dagger, d_\mu^\dagger \mapsto \alpha_s^*, \alpha_\mu^*$ in the respective normal-ordered quantal expressions.

Since Glauber coherent states do not fix the total number of bosons, an additional constraint must be required, namely $\langle \alpha | \hat{N} | \alpha \rangle = |\alpha_s|^2 + \sum_\mu |\alpha_\mu|^2 = N$. This (plus an arbitrary choice of the overall phase, $\alpha_s = \sqrt{N - \sum_\mu |\alpha_\mu|^2}$) reduces the number of relevant degrees of freedom from six to five. Naturally, the classicality of coherent states becomes more and more pronounced as N increases and the fully classical limit is obtained in the $N \rightarrow \infty$ limit. To prevent divergence of the corresponding averages, one has to scale all operators according to their order [see the $\frac{1}{N^k}$ factors in Hamiltonian (1)] and to absorb the respective factors into the definition of α 's. This leads to the substitution $\alpha_\mu \mapsto \tilde{\alpha}_\mu = \frac{\alpha_\mu}{\sqrt{N}}$ while, simultaneously, the $\frac{1}{N^k}$ factors drop out.

Final expressions for the classical-limit observables are obtained after the identification of real coordinates q_μ

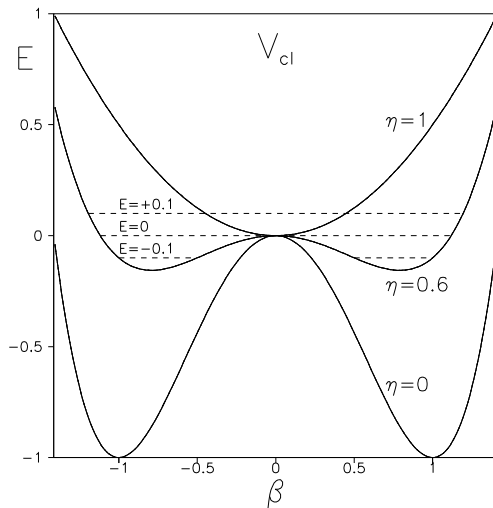


FIG. 1: Potential energy term of Hamiltonian (3) for three values of parameter η . The lowermost ($\eta = 0$) and uppermost ($\eta = 1$) curves correspond to O(6) and U(5) limits, respectively. The middle curve ($\eta = 0.6$) represents an intermediate case, for which the accessible range of radii (for the three given energies) is shown by the dashed lines. “Negative radii” express the $(\beta, \gamma) \rightarrow (\beta, \gamma + 180^\circ) \equiv (-\beta, \gamma)$ transformation and are included just to emphasize the rotational symmetry.

and momenta p_μ via relations $\sqrt{2}\tilde{\alpha}_\mu = (-)^\mu q_{-\mu} + ip_\mu$ and $\sqrt{2}\tilde{\alpha}_\mu^* = q_\mu - (-)^\mu ip_{-\mu}$. The coordinates q_μ are associated with the geometric variables describing an instantaneous quadrupole deformation of the nucleus and its orientation in the laboratory frame. Due to the fixed boson number average, the motion is constrained by the condition

$$\sum_\mu (p_\mu^2 + q_\mu^2) \leq 2 \quad (2)$$

to the interior of a sphere in the 10-dimensional phase space.

The calculation of classical observables is substantially simplified for zero angular momentum, $l = 0$ [12, 15]. In this case, the intrinsic frame connected with the ellipsoid of deformation remains at rest and one can fix $\text{Re } q_0 \equiv x$, and $\text{Re } q_{+2} = \text{Re } q_{-2} \equiv y/\sqrt{2}$ (while $q_{\pm 1} = \text{Im } q_{\pm 2} = \text{Im } q_0 = 0$). The $l = 0$ classical limit of Hamiltonian (1) reads as

$$H_{\text{cl}} = \underbrace{\frac{\eta}{2} \pi^2 + (1 - \eta) \beta^2 \pi^2}_{T_{\text{cl}}} + \underbrace{\frac{5\eta - 4}{2} \beta^2 + (1 - \eta) \beta^4}_{V_{\text{cl}}}, \quad (3)$$

where $\beta^2 = x^2 + y^2$ is the squared radius in the $q_0 \times \sqrt{2}q_{\pm 2}$ plane (the polar angle denoted as γ) and π^2 the squared length of the associated vector of momenta:

$$\pi^2 = \pi_x^2 + \pi_y^2 = \pi_\beta^2 + \left(\frac{\pi_\gamma}{\beta}\right)^2. \quad (4)$$

Hamiltonian (3) can be thought to describe planar motions of a particle with the position-dependent kinetic

energy T_{cl} in potential V_{cl} , which is for $\eta = 0, 0.6$ and 1 shown in Figure 1. While for $\eta < \eta_c = \frac{4}{5}$, the potential has the “Mexican hat” (or “champagne bottle”) form, for $\eta \geq \eta_c$ it is just a well with minimum at $\beta = 0$. To emphasize the rotational symmetry in the $x \times y$ plane, we show both positive and “negative” domains of β (the latter corresponding to the rotation by angle 180°). As follows from the form of the potential and from Eq. (2), the radius must satisfy

$$\beta \in [\beta_{\min}, \beta_{\max}] \subset [0, \sqrt{2}] \quad (5)$$

and the total energy

$$E \in [E_{\min}, E_{\max}] \subset [-1, +1], \quad (6)$$

$$E_{\min} = \begin{cases} -\frac{(5\eta-4)^2}{16(1-\eta)} & \text{for } \eta < \frac{4}{5} \\ 0 & \text{for } \eta \geq \frac{4}{5} \end{cases}, \quad E_{\max} = \eta.$$

Remind that throughout this paper the energy is always expressed in units of the scaling constant a , see Eq. (1), so it is formally dimensionless.

Note that polar coordinates β and γ of x and y can be immediately associated with Bohr geometric variables, but in this case the deformation parameter would be restricted to $\beta \in [0, \sqrt{2})$. To obtain $\tilde{\beta} \in [0, \infty)$, as is usual in nuclear structure, the coordinate plane must be radially stretched [16] according to $\beta \mapsto \tilde{\beta} = \frac{\beta}{\sqrt{2-\beta^2}}$. Ex-

pressed in new polar coordinates $(\tilde{\beta}, \gamma)$ and the associated momenta $(\tilde{\pi}_\beta, \pi_\gamma)$, Hamiltonian (3) transforms into the following form:

$$H_{\text{cl}} = \frac{1}{4} \left[\eta + (4 - 3\eta)\tilde{\beta}^2 \right] \left[(1 + \tilde{\beta}^2)^2 \tilde{\pi}_\beta^2 + \left(\frac{\pi_\gamma}{\tilde{\beta}} \right)^2 \right] + \frac{(5\eta - 4)\tilde{\beta}^2 + \eta\tilde{\beta}^4}{(1 + \tilde{\beta}^2)^2}. \quad (7)$$

Here, the upper physical limit of energy, E_{\max} , is reached when the motion becomes infinite. In the following, we will use the classical limit in the form of Eq. (3), i.e., with β restricted to the finite interval (5).

It is immediately apparent that the Hamiltonian in Eqs. (3) and (7) is “ γ -soft”, invariant under rotations about the origin, so it conserves the “angular momentum”

$$\pi_\gamma = x\pi_y - y\pi_x. \quad (8)$$

Thus, since the number of degrees of freedom $f = 2$, the system must be integrable. This is in agreement with the arguments explaining the integrability of the $[\text{O}(6)-\text{U}(5)] \supset \text{O}(5)$ Hamiltonians with arbitrary angular momenta, as outlined in Part I [1], since Eq. (8) is closely related to the integral of motion $\hat{C}_2[\text{O}(5)] = \frac{1}{5}(\hat{L} \cdot \hat{L}) + 2(\hat{T}_3 \cdot \hat{T}_3)$. Indeed, for $l = 0$ the classical limit of the $\text{O}(5)$ Casimir invariant reads as [9]:

$$C_2[\text{O}(5)]_{\text{cl}} \Big|_{l=0} = 2\pi_\gamma^2. \quad (9)$$

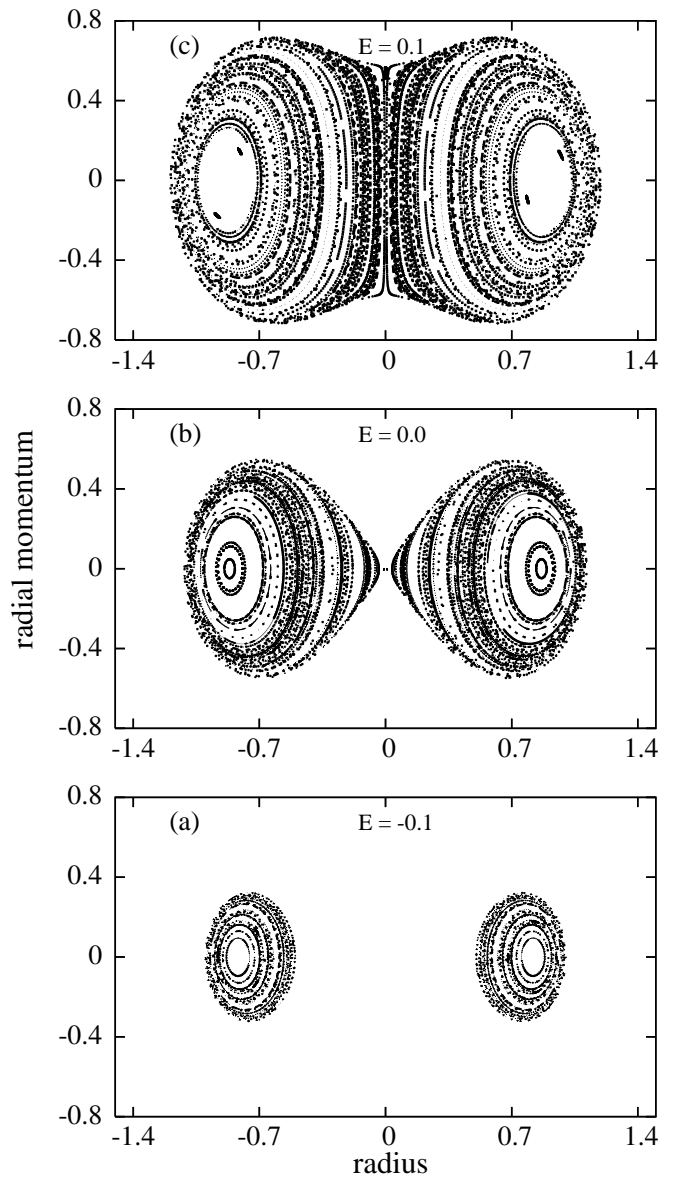


FIG. 2: Poincaré phase-space sections for Hamiltonian (3) with $\eta = 0.6$ at the three given values of energy (panels a-c). The sections show a finite number of crossings of 10 (a), 30 (b), and 50 (c) trajectories with the plane $\beta \times \pi_\beta$ for arbitrary γ .

Note that since “angular momentum” (9) does not correspond to ordinary $\text{O}(2)$ algebra of two-dimensional rotations, its quantization yields eigenvalues $v(v+3)$, where for $l = 0$ the seniority takes values $v = 0, 3, 6, \dots$, in contrast to the m^2 formula with $m = 0, \pm 1, \pm 2, \dots$ corresponding to $\text{O}(2)$. Nevertheless, we realize that each value of $C_2[\text{O}(5)]_{\text{cl}}$ is associated with both signs of π_γ , i.e., with two opposite orientations of the motion in γ -direction. This intrinsic “degeneracy” (which does not affect physical results in the quantum case) will become important in Sec. IV.

The integrability of Hamiltonian (3) is illustrated in

Figure 2, where we show Poincaré phase-space sections for $\eta = 0.6$ at three different energies, (a) $E = -0.1$, (b) $E = 0$, and (c) $E = 0.1$. Each of the panels represent passages of 10–50 randomly selected trajectories with the given energy E through the $\beta \times \pi_\beta$ plane in the 4-dimensional phase space. Due to the rotational symmetry, the plane can have an arbitrary orientation in the $x \times y$ frame and the pattern of sections must be symmetric under the reflection of the β axis (we show both $\beta > 0$ and “ $\beta < 0$ ” halves).

All sections in Fig. 2 demonstrate fully regular dynamics, in agreement with the integrability of our system. As can be anticipated from Fig. 1, the $E < 0$ motions in panel (a) must be confined inside the annular region $\beta \in [\beta_{\min}, \beta_{\max}]$, while the $E > 0$ trajectories in panel (c) already range over the full disc $\beta \in [0, \beta_{\max}]$ (the values β_{\min} and β_{\max} depend on energy). Panel (b) shows just the singular $E = 0$ situation, when the central inaccessible (for $E < 0$) disc shrinks into a single point (which can be reached in infinite time). We will return to this case in Sec. IV.

Let us stress that the Poincaré sections in Fig. 2 separate trajectories with different energies, but mix together those with various values of the angular momentum π_γ . Indeed, the outermost curves in all panels represent pure β -vibrations with $\pi_\gamma = 0$, while the central points (not shown) correspond to “spinning” only in the γ -direction with $\pi_\beta = 0$. The other trajectories correspond to various mixtures of β - and γ -vibrations. An interesting attribute of these intermediate cases is the spread $\Delta\beta$ of each individual trajectory in the β -direction, which can be determined as the difference between radii corresponding to the outermost and innermost points. This will be used in Sec. III to classify quasiperiodic orbits in our system.

III. PERIODIC ORBITS

A. Berry-Tabor formula, singular orbits, and bifurcations

Semiclassical analyses of quantal spectra are performed in the framework of so-called trace formulas which represent the fluctuating part $\varrho_{\text{fl}}(E)$ of the level density $\varrho_{\text{tot}} = \varrho_{\text{sm}} + \varrho_{\text{fl}}$ in terms of purely classical quantities associated with periodic orbits, while the complementary smooth part $\varrho_{\text{sm}}(E)$ is determined just as the classical phase-space volume available at a given energy E in units of \hbar^f (where f is the number of system’s degrees of freedom). The best known expression, derived by Gutzwiller [5], was obtained under the assumption that individual periodic orbits are isolated, which is not satisfied for integrable systems. In this case, periodic orbits come in continuous families characterized by arbitrary shifts of initial angles if the motion is described in the action-angle variables [13]. An adequate semiclassical approach to the level density of integrable systems was developed by Berry and Tabor [7].

In the following, we consider a two-dimensional integrable system, $f = 2$, which applies in our case of Hamiltonian (3). In the action-angle representation the Hamiltonian depends only on actions, $H = H(I_1, I_2)$, and the angles evolve according to $\dot{\theta}_1 = \omega_1$ and $\dot{\theta}_2 = \omega_2$. All trajectories represent folded rotations on various tori determined by $\vec{I} = (I_1, I_2)$. Let us note that in many integrable systems, including ours, the action-angle variables can only be introduced locally [14] (cf. Sec. IV). Therefore, it is not possible to write down analytic expressions for the corresponding canonical transformation from normal coordinates and momenta.

Any primitive periodic orbit on a given torus can be characterized by a pair of coprime integers $(\mu_1, \mu_2) \equiv \vec{\mu}$ such that the ratio of angular frequencies $\mathcal{R} = \frac{\omega_1}{\omega_2}$ coincides with the rational number $\frac{\mu_1}{\mu_2}$. The Berry-Tabor formula for the fluctuating part of the quantal state density [7] then reads as

$$\varrho_{\text{fl}}(E) = \frac{1}{\pi\hbar} \sum_{\vec{\mu}} \sum_{r=1}^{\infty} \frac{T_{\vec{\mu}}}{\sqrt{\hbar|g''_E|(r\mu_2)^3}} \times \cos \left[\frac{1}{\hbar} r S_{\vec{\mu}}(E) - \frac{\pi}{2} r \nu_{\vec{\mu}} - \frac{\pi}{4} \right], \quad (10)$$

where the sum runs over all repetitions r of all primitive orbits $\vec{\mu}$ with period $T_{\vec{\mu}} = \frac{2\pi\mu_1}{\omega_1} = \frac{2\pi\mu_2}{\omega_2}$, Maslov index $\nu_{\vec{\mu}}$ [3], and action

$$S_{\vec{\mu}}(E) = 2\pi\vec{I} \cdot \vec{\mu} = \int_0^{T_{\vec{\mu}}} [\pi_\beta \dot{\beta} + \pi_\gamma \dot{\gamma}] dt. \quad (11)$$

The meaning of the function g''_E in Eq. (10) will be explained later.

Expression (11), which in the general case integrates the scalar product of momentum and velocity over the specific periodic trajectory $\vec{\mu}$, has a particularly simple form for billiards (or cavities), where one can write $S_{\vec{\mu}} = 2ET_{\vec{\mu}} = pL_{\vec{\mu}}$ with $p = mv$ denoting the ordinary momentum and $L_{\vec{\mu}}$ the length of the given orbit. For “soft” systems, the dependence of $S_{\vec{\mu}}$ on energy is nonlinear and frequencies of individual cosine terms in Eq. (10) vary with E . Since in the latter case each oscillatory term in the Berry-Tabor formula contains also a nontrivial energy dependence of the amplitude, the semiclassical analysis of spectra in such cases is certainly much less intuitive than in the hard-wall systems.

In general, there may exist singular orbits with diverging contributions to the Berry-Tabor formula. This happens if either the period of the given orbit grows to infinity, $T_{\vec{\mu}} \rightarrow \infty$, or if the denominator of the prefactor in Eq. (10) vanishes, $g''_E \rightarrow 0$. The former case applies to the motions that for some energy become infinitely slow at a certain point, which can be associated with an unstable equilibrium of the system. We know from the discussion in Sec. II that our system contains such a point, namely the central maximum of the potential in Eq. (3) at $\beta = 0$ for $\eta \leq \frac{4}{5}$. For trajectories with $E = 0$,

this maximum can only be reached in asymptotic times because the force vanishes there. Among the trajectories passing this point there are also various periodic orbits, whose contribution to Eq. (10) must diverge at $E = 0$ because of the period tending to infinity. This is essentially the classical mechanism responsible for the bunching of quantum levels in the region $E \approx 0$, see Fig. 1 in Part I [1]. It shows that the bunching pattern is not just a finite- N quantum fluctuation, but a robust effect deeply ingrained in the classical limit of the system. Theoretical foundations underlying the existence of the singular class of trajectories and another approach to understand their influence on the quantum spectrum will be discussed in Sec. IV.

The second possible source of infinite contributions to the Berry-Tabor formula (10) is connected with the cases when $g''_E(I_1) \equiv \frac{\partial^2 g_E}{\partial I_1^2}(I_1) = 0$. The function $g_E(I_1)$ is determined [17] from the implicit equation $H(I_1, I_2 = g_E) = E$, which after differentiation and the use of Hamilton equations yields

$$\dot{\theta}_1 + \dot{\theta}_2 \frac{\partial g_E}{\partial I_1} = 0, \quad (12)$$

so that $g'_E = -\frac{\omega_1}{\omega_2} = -\mathcal{R}$. In other words, the function g_E matches possible pairs of actions (I_1, I_2) , i.e., selects the tori \vec{I} relevant at a given energy, and its first derivative determines the corresponding frequency ratios. If $-g'_E$ is rational, for a selected torus, the associated orbit is periodic and contributes to Eq. (10). The second derivative g''_E measures the change of \mathcal{R} as one steps to the tori in an infinitesimal vicinity of \vec{I} . If $g''_E \neq 0$, the periodic orbit $\vec{\mu}$ on the torus \vec{I} does not survive the transition to $\vec{I} + \delta\vec{I}$. If, however, $g''_E = 0$, a family of periodic orbits with the same frequency ratio \mathcal{R} exists in neighboring tori, which results in diverging contribution to the Berry-Tabor formula (10).

Note that the Gutzwiller formula [5], which is valid in nonintegrable systems with isolated periodic orbits, is formally similar to Eq. (10), but with the prefactor denominator replaced by $\sqrt{\det[(M_p)^r - 1]}$, where M_p stands for the so-called monodromy matrix of a given primitive periodic orbit p [3, 4]. This matrix describes the stability of orbit p in terms of linearized deviations from the given phase-space trajectory under a perpendicular perturbation of its initial point. Thus $(M_p)^r - 1$ represents the deviation from the perturbed phase-space position after r repetitions. If one (or more) of the eigenvalues of this matrix is equal to zero, i.e., if $\det[(M_p)^r - 1] = 0$, there exists at least one direction in the phase space in which any deviation from the given orbit $r \cdot p$ results in another periodic orbit. The new orbits are detached from the primitive orbit p as its period r -tupling clones. Consequently, p is not isolated and the corresponding term in the Gutzwiller formula diverges. This situation is analogous to the one with $g''_E = 0$, as described above.

Both the above singular cases correspond to the same general phenomenon, called bifurcation [18]. In Hamil-

ton systems of classical mechanics, bifurcations represent branching of periodic orbits at some critical values of energy or other parameters [13]. While periodic orbits existing below and above the given bifurcation energy E_b are isolated, either in the sense of $g''_E \neq 0$ or $\det[(M_p)^r - 1] \neq 0$, at $E = E_b$ two or more orbits merge together in the way described above, giving rise to zero denominators of the respective semiclassical level-density formulas. At the bifurcation energies E_b , the Berry-Tabor or Gutzwiller formulas do not represent correct approximations of the fluctuating level density. Improved semiclassical methods were developed to treat these situations [19]. Intuitively one expects an enhancement of the level-density oscillations at the bifurcation points. In the following subsection we will show that in our system numerous bifurcations of periodic orbits take place in the energy range $E > 0$.

B. Numerical results

We have performed a numerical analysis of classical motions corresponding to Hamiltonian (3) in the interval of energies $E \in [-0.1, +0.3]$ using a sample of about 50000 generated orbits. Individual trajectories were calculated with initial positions and momenta chosen randomly within the phase-space region accessible at a given energy and classified by the ratio

$$R = \frac{T_\gamma}{T_\beta} = \frac{\langle \omega_\beta \rangle}{\langle \omega_\gamma \rangle} \quad (13)$$

of periods T_γ and T_β associated with oscillations in both γ and β directions, respectively. Since $\omega_\gamma = \dot{\gamma}$ and the angular velocity ω_β connected with β -vibrations are both time dependent, one has to use the corresponding average angular frequencies per period, $\langle \omega_\gamma \rangle = \frac{2\pi}{T_\gamma}$ and $\langle \omega_\beta \rangle = \frac{2\pi}{T_\beta}$. Their inverse ratio coincides with R and is analogous to the above-discussed ratio $\mathcal{R} = \frac{\omega_1}{\omega_2}$ of frequencies in the action-angle variables. In particular, rational values $R = \frac{\mu_\beta}{\mu_\gamma}$ correspond to periodic orbits with period $T_{\mu_\beta/\mu_\gamma} = \mu_\beta T_\beta = \mu_\gamma T_\gamma$.

Examples of periodic orbits with various rational values of the ratio (13) are shown in Figure 3. The rational fraction $R = \frac{\mu_\beta}{\mu_\gamma}$ classifying the given orbit has visual meaning as the number of outer return points of the β -vibration over the number of rotations in the γ -direction needed to close the orbit. Thus, for instance, the 5/2 orbits look like stars with 5 outer ‘‘points’’ that close in 2 rotations, while the 5/1 stars are similar, but close only in 1 rotation. The outer and in some panels also the inner circles in Fig. 3 demarcate the energetically accessible areas $\beta \in [\beta_{\min}, \beta_{\max}]$ in the $x \times y$ plane. As discussed in Sec. II, this area is a disc for $E > 0$, an annular ring for $E < 0$, and a disc minus the central point for $E = 0$. We see that although the orbits in Fig. 3 do not just trivially bounce between the outer (and inner) limits, as in the case of circular or annular infinite sharp wells, they still

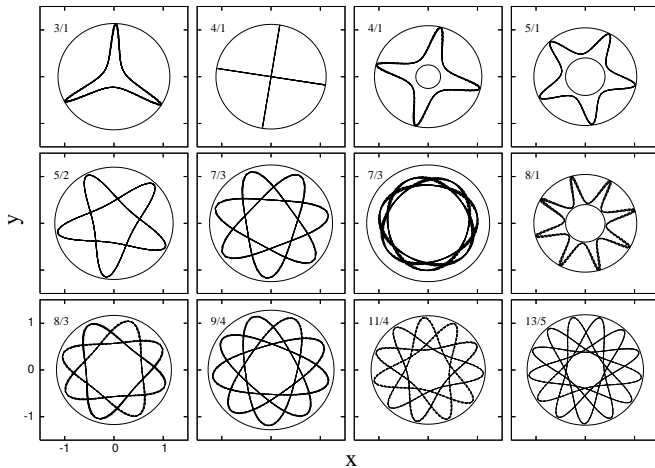


FIG. 3: Examples of various periodic orbits at different energies for Hamiltonian (3) with $\eta = 0.6$ and their classification by rational fractions $R = \frac{\mu_\beta}{\mu_\gamma}$.

resemble to a large extent the trajectories in these simple systems [20].

Periodic orbits form a dense subset of all allowed motions and we therefore need a more complete picture. A histogram showing the occurrence of trajectories with arbitrary (rational or irrational) values of the frequency ratio R within the whole sample of trajectories with $E \in [-0.1, +0.3]$ is presented in Figure 4. For each value of energy within the given range (the energy step was chosen $\Delta E = 0.01$), the sample contains $N_{\text{tot}} = 1200$ trajectories and Fig. 4 depicts their distribution (numbers N_{tr} of trajectories) into bins of size $\Delta R = 0.01$ along the R -axis.

The structure shown in Fig. 4 discloses rather interesting features of classical motions. For each energy, the orbits occur within a band

$$R \in [R_{\min}(E), R_{\max}(E)] \quad (14)$$

of allowed frequency ratios. The lower bound $R_{\min}(E)$ gradually decreases with increasing energy for $E < 0$, but it is constant, $R_{\min} = 2$, for $E > 0$. Because of the limited precision inherent in our generated sample of trajectories (with nonzero values of the bin size ΔR and energy step ΔE) we cannot resolve whether the $R_{\min}(E)$ dependence is discontinuous or just nonanalytic at $E = 0$. In any case, the curve reaches the minimal value at this point. On the other hand, for energy approaching the minimum E_0 of the potential in Eq. (3) (this energy is below the range displayed in Fig. 4) we must have $R_{\min} \rightarrow \infty$. The upper bound of interval (14) is also a decreasing function of energy which passes the value $R_{\max} = 4$ at $E = 0$. The decrease of $R_{\max}(E)$ for $E < 0$ (and partly also just above $E = 0$) is so steep that it cannot be resolved with the present energy step, but we assume that it is a smooth curve. It is obvious that a very narrow energy interval around the point $E = 0$ carries the most substantial changes in the spectrum of orbits, where

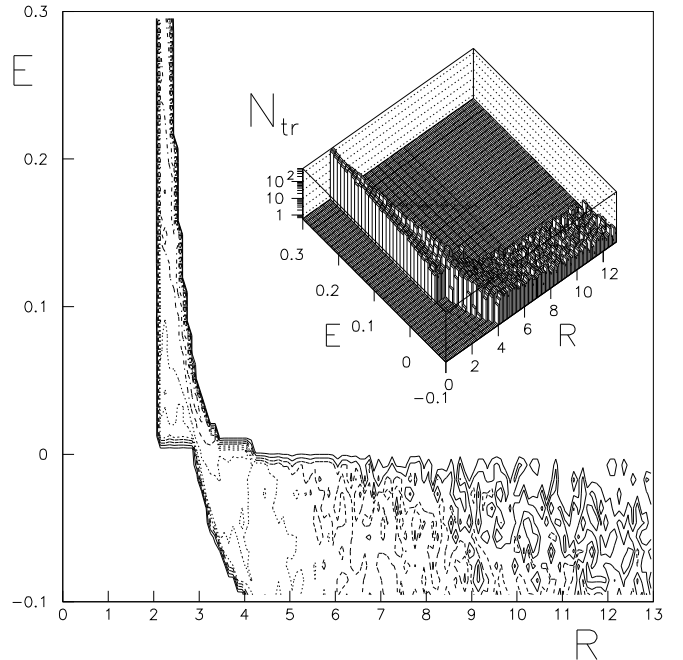


FIG. 4: Frequency of occurrence of trajectories with different ratios R for Hamiltonian (3), $\eta = 0.6$, in the reference sample of trajectories with different energies. For each value of E (step $\Delta E = 0.01$) there was 1200 generated trajectories and the histogram (see the inset) shows their distribution in R (the bin width $\Delta R = 0.01$). The main diagram (contour plot of the logarithmic histogram) depicts the band structure of allowed R values, see Eq. (14) and below.

the trajectories pass between both negative and positive energy regions just through a bottleneck of values $R \in [3, 4)$. While for $E < 0$ the orbits look similar to those in the $O(6)$ limit, for $E > 0$ they already resemble the $U(5)$ limit.

The behavior demonstrated in Fig. 4 can be qualitatively understood from the change of the energetically accessible $x \times y$ area around $E \approx 0$. The form of annular ring, valid for $E < 0$, does not support trajectories with $R < 3$ since these have to traverse through the central region. Consequently, these trajectories can only exist for $E > -\varepsilon$, where $\varepsilon \approx 0.03$. On the other hand, the central reflecting disc is needed for trajectories with $R \geq 4$, which therefore appear only for $E < 0$. One can say that the $R \in [4, \infty)$ trajectories, which are “bouncing” between inner and outer circles inside the annular region for $E < 0$, transform to the straight $R \in [2, 3]$ trajectories at $E \approx 0$ where the central disc gradually disappears and the accessible domain of deformation parameters becomes simply connected. Note that the rapidity of changes of classical motions around zero energy is connected with the fact that for $E \rightarrow 0_-$ the radius of the central disc converges to zero with a rate increasing to infinity ($\beta_{\min} \propto \sqrt{-E}$), as directly follows from the form of the potential V_{cl} close to the $\beta = 0$ maximum.

Figure 5 shows the relative frequency of occurrence of

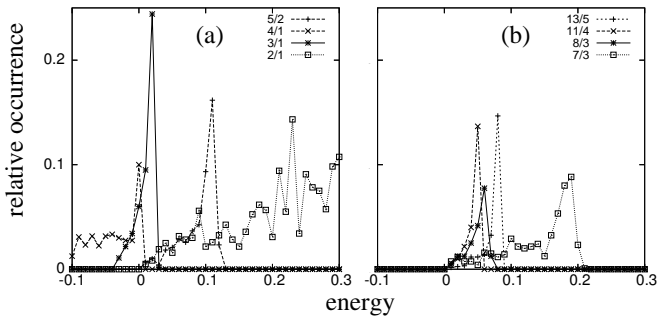


FIG. 5: Relative frequency of occurrence of several types of quasiperiodic orbits (see Fig. 3) for $\eta = 0.6$ as a function of energy. The scale on the vertical axis depends on the value $\Delta\gamma$ in Eq. (15), here equal to 5° .

several types of *periodic* orbits from Fig. 3 in our generated sample as a function of energy. The curves in Fig. 5 can be basically understood as energy cuts of the function N_{tr} in Fig. 4 at the respective rational values $R = \frac{\mu_\beta}{\mu_\gamma}$ of the fraction (13), but with a variable precision ΔR . More specifically, Fig. 5 presents the relative fraction of all generated (at each energy) trajectories satisfying the condition that the μ_β th outer reflection after μ_γ revolutions is shifted from the 1st outer reflection by an angle not exceeding (in absolute value) the selected precision $\Delta\gamma = 5^\circ$. This leads to the condition

$$\left| \frac{R - \frac{\mu_\beta}{\mu_\gamma}}{R} \right| \leq \frac{\Delta\gamma}{2\pi\mu_\gamma}. \quad (15)$$

Let us stress that the use of a smaller value of $\Delta\gamma$ decreases the yield of trajectories—implying a prolongation of the computation time—but does not change (as we checked for $\Delta\gamma = 1^\circ$) the shape of dependences in Fig. 5.

The most common type of behavior shown in Fig. 5 indicates that for many orbits the relative frequency of occurrence sharply culminates at a certain energy, just before this orbit totally disappears from the system. The sharpest peak of this kind is observed at $E = 0.02$ for the 3/1 orbits, but there are also other well pronounced peaks, like the 5/2, 11/4, or 13/5 ones, and many others. All these maxima appear at positive energies and one can trace their origin to the ridge of values N_{tr} visible for $E > 0$ at the upper bound $R_{\text{max}}(E)$ in Fig. 4 (see the inset). The peak at $E = 0$ (the 4/1 “crosses”) and also the one at $E = 0.02$ (the 3/1 “Mercedes-Benz stars”, see Fig. 3) are located just on the upper edge of the major $E \approx 0$ level bunching pattern in Fig. 1 of Part I [1].

Special attention should be paid to the 4/1 orbits that in our system take two different forms: For $E < 0$ they exist as stars, shown in the third uppermost panel of Fig. 3, but at $E \approx 0$ they can also look like crosses, see the second panel. (In fact, the latter case exemplifies the above-discussed critical $E = 0$ periodic trajectories with infinite period, as will be further elaborated in Sec. IV.) The contributions of these forms to the dependence in

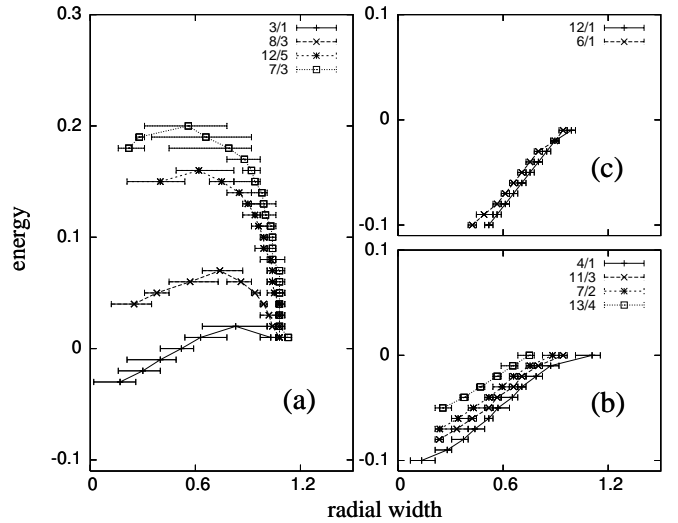


FIG. 6: The radial width $\Delta\beta$ of individual periodic orbits $\frac{\mu_\beta}{\mu_\gamma}$ as a function of energy ($\eta = 0.6$). Horizontal bars at each energy demarcate intervals of $\Delta\beta$ where trajectories are detected within our sample, while points connected by curves represent statistical averages within each interval. The bifurcations of orbits in panel (a) explain the respective peaks in Fig. 5.

Fig. 5(a) can be decomposed into a constant step-like function equal to zero for $E > 0$ (“stars”) and a sharp peak at $E = 0$ (“crosses”).

We also see in Fig. 5(a) that the 2/1 orbits, which pass via the central maximum of the potential and correspond to the $E > 0$ edge R_{min} in Fig. 4, exhibit a different type of energy dependence than the others. The frequency of occurrence of these orbits is zero at $E \leq 0$ and gradually increases (if neglecting fluctuations) with energy $E > 0$.

It is not difficult to show that the peaks in Fig. 5 corresponding to the $R \in (2, 3]$ orbits are connected with bifurcations. To this end, we first characterize individual orbits by the radial width, defined as the difference $\Delta\beta$ between the outer and inner radii (see the end of Sec. II). The values of $\Delta\beta$ associated with various orbit types are shown in Figure 6, where the horizontal bars demarcate intervals of the $\Delta\beta$ values which are populated (for energy given on the vertical axis) by some trajectories in our sample. The curves (used just to lead the eye) connect points that represent arithmetic averages of $\Delta\beta$ in neighboring intervals.

The three panels of Fig. 6 collect three types of qualitatively different behaviors: (a) For $R \in (2, 3]$, the populated domain of $\Delta\beta$ consists of two separate branches (see, e.g., the two 7/3 orbits in Fig. 3) that merge at a certain energy $E_b(R) > 0$, which can be determined from the condition $R_{\text{max}}(E_b) = R$. Similarly, the lower endpoint energy (the termination of the longer branch of the respective curve) follows from the $R_{\text{min}}(E)$ bound. (b) For $R \in (3, 4]$, the domains consist of only one band that shifts to larger $\Delta\beta$ values as the energy increases and

terminates slightly above $E = 0$. The upper endpoint energies can again be determined from $R_{\max}(E)$, but as discussed above, this dependence is so steep in the given range of R that all endpoint energies in Fig. 6(b) fall into the narrow interval $E \in [0, 0.01]$. Lower endpoint energies again follow from $R_{\min}(E)$. A special case of this kind is the 4/1 orbit with the two above-discussed incarnations (see Fig. 3): the respective $\Delta\beta$ value at the endpoint $E = 0$ is apparently deviated from the direction followed for $E < 0$. (c) For $R > 4$, the $\Delta\beta$ bands look similar as in case (b), but terminate at energies just below $E = 0$, supposedly following the steep $E < 0$ branch of the curve $R_{\max}(E)$.

It becomes apparent that the $R \in (2, 3]$ peaks in Fig. 5 arise due to the merge of two different branches of $\Delta\beta$ values, as shown in Fig. 6(a). An increased frequency of occurrence of the orbit just before the endpoint is related to the flatness of the respective curve close to its maximum (a larger number of trajectories is concentrated in a smaller energy interval). At the endpoint ($\Delta\beta_b, E_b$) of each of the curves in Fig. 6(a) the respective type of periodic orbit bifurcates, having infinitely close neighbors with different radial widths, and thus yields $g'_E = 0$, as discussed in Sec. III A. The Berry-Tabor formula (10) cannot be applied at these points [19]. In our case, the bifurcations seem to be of the pitchfork type, when two stable orbits join and produce an unstable one [18]. Unfortunately, the unstable orbits are not accessible to numerical studies, so they are not seen in Fig. 6. This problem may be further investigated analytically.

It follows from the above discussion that the bifurcations are connected only with the region of positive energies (there is a ridge of N_{tr} values, apparent in the inset of Fig. 4, which is located solely at the $R_{\max}(E)$ edge with $E > 0$). This implies that divergences of the Berry-Tabor formula associated with bifurcations are not directly relevant in the explanation of the main level-bunching pattern in Fig. 1 of Part I [1] (except perhaps the 3/1 case with $E_b = 0.02$). Bifurcation energies for low-period orbits are not even correlated with the secondary, less pronounced bunchings of levels, observed in the region $E > 0$ [1]. Therefore, it seems that the presence of various orbits in the same energy range and an interplay of their bifurcations result in interferences that wash out contributions of individual orbits.

On the other hand, highly organized behavior of levels at $E \approx 0$ perfectly coincides with the predicted existence of a singular torus of orbits with infinite period at zero energy, and also with the observed abrupt redistribution of the spectrum of orbits in a narrow vicinity of this energy.

IV. CLASSICAL AND QUANTUM MONODROMY

The anomalous $E = 0$ bundle of orbits with infinite period, discussed in Sec. III A, is related to a more general

phenomenon, called monodromy. Classical monodromy in integrable Hamilton systems can be briefly introduced as the impossibility to define global action-angle variables due to the existence of a singular, so called “pinched” torus [14]. The name *Μονοδρομία* (“once around”) originates from a property similar to that of the Möbius strip: if one follows a closed loop in the space of regular tori around the singular torus and—loosely speaking—redefines the coordinate system on the consecutive tori continuously on the way along the loop, one returns back to the starting torus with a coordinate system that differs from the initial one.

Classical monodromy affects the quantum counterpart of the system via the Einstein-Brillouin-Kramers (EBK) quantization rules [3, 4]. It turns out that quantum monodromy can be seen as a point defect in the lattice of quantum numbers corresponding to a complete set of commuting operators. This defect results in a transformation of the elementary quantum cell when a closed loop is completed around the singular point, in analogy with the above feature of phase-space tori. An overview of the mathematical background and various examples of monodromy can be found in Ref. [21].

Soon after its discovery in 1980 [22] it became clear that monodromy substantially affects global features of numerous integrable systems, which might previously be considered as too trivial for detailed analyses. The simplest system that exhibits monodromy is the spherical pendulum—particle moving on a sphere in a gravitational field. It can be shown [14, 21] that the phase-space torus passing the unstable equilibrium position at the north pole, with the particle energy exactly equal to the critical value E_m needed to reach that point, is pinched, i.e., one of its basic circles is contracted to a single point (with appropriate initial conditions the particle is at rest). As a consequence, the lattice of quantum states, characterized by quantum numbers enumerating energy E and the projection L_z of angular momentum, has a point defect at $(E, L_z) = (E_m, 0)$. It was found that closely related to this simple observation is the realization of monodromy in vibrational and rotational spectra of some molecules [21, 23].

Other examples of monodromy can be found in the following systems: particle in quartic, sextic, and decatic potentials [24], hydrogen atom in orthogonal electric and magnetic fields [25], systems of two or three coupled angular momenta [26], particle bouncing between walls in a prolate elliptic cavity [27] or moving in a two-center attractive potential [28]. Like in the spherical pendulum, monodromy in several of the latter systems is connected with the trajectories passing with the critical energy via the point of an unstable equilibrium [21, 24, 28]. We already know that a similar point, namely the top of the central maximum at $\beta = 0$, can be found in our classical Hamiltonian (3) for $\eta \leq \eta_c \equiv \frac{4}{5}$, with $E_m = 0$ being the minimal energy needed to pass through this point. In fact, our Hamiltonian for $\eta \leq \eta_c$ is identical with the “champagne-bottle” Hamiltonian of Ref. [24], except the

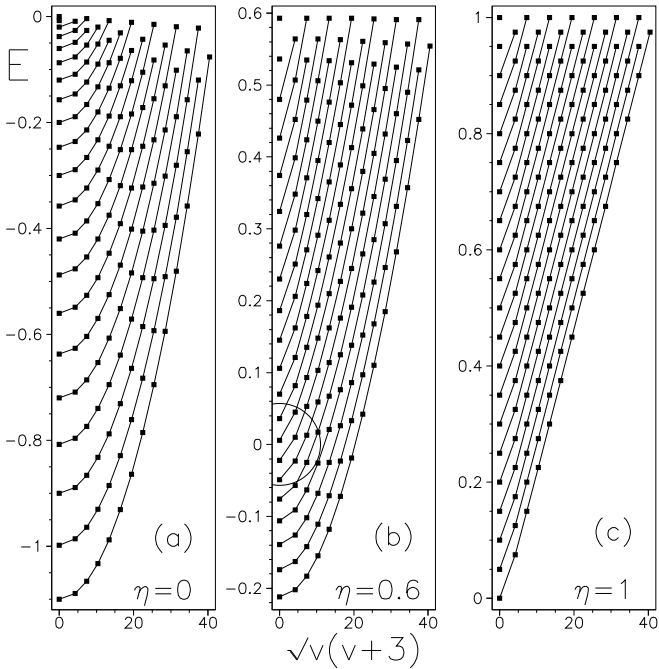


FIG. 7: The lattice of $l = 0$ eigenstates of Hamiltonian (1) with three given values of η (panels a–c) and $N = 40$ in the plane $E \times \sqrt{v(v+3)}$ (where the seniority $v = 0, 3, 6, \dots$). Lines connect states with the same radial quantum numbers n_β . The singular torus $(E, v) = (0, 0)$ is located in the center of the semicircle in panel (b).

position-dependent kinetic term in Eq. (3), which however does not affect the presence of monodromy with the central point $(E, \pi_\gamma) = (0, 0)$.

Figure 7 shows the lattice of $l = 0$ eigenstates of quantum Hamiltonian (1) with the number of bosons $N = 40$ in the plane where the vertical axis represents energy E and the horizontal axis the momentum

$$\pi_\gamma \equiv \sqrt{v(v+3)} = 3\sqrt{\tilde{v}(\tilde{v}+1)}. \quad (16)$$

Since for zero angular momentum the seniority takes values equal to multiples of 3, we defined above also the “reduced” seniority quantum number $\tilde{v} \equiv \frac{v}{3} = 0, 1, 2, \dots$. The three panels in Fig. 7 correspond to various values of the control parameter: (a) $\eta = 0$, the O(6) case, (b) $\eta = 0.6$, a transitional case, and (c) $\eta = 1$, the U(5) case. Individual states (marked by dots) can be directly related to level energies at the respective values of η in Fig. 1 of Part I [1], which collects all states with different seniorities for the same boson number as here.

Sorting of states according to seniority in Fig. 7 helps to identify the values of v that are involved in level bunchings at different points η . For instance, one immediately sees that the clustering of levels across the whole spectrum in the U(5) limit (panel c) is due to the multiple degeneracy of states with even or odd values of \tilde{v} , that correspond to the same value of the U(5) quantum number n_d (even or odd, respectively). For the highest states, this degeneracy remains approximately valid across the

whole interval $\eta \in [0, 1]$, see panels (a)–(c). The seniority deconvolution of the spectrum for $\eta < \frac{4}{5}$ is exemplified by the $\eta = 0.6$ case in panel (b). We observe here that levels with all values of \tilde{v} become nearly degenerate in the region around zero energy, which is a clear signature of the $E \approx 0$ bunching pattern [1].

The lattices in Fig. 7 represent quantum energy-momentum maps [21] of the classical phase space, with each dot being an image of a classical torus of trajectories that survived the semiclassical EBK quantization [17]. This is given by $I_i = 2\pi\hbar(n_i + \frac{\nu_i}{4})$, where I_i (with $i = 1, 2$) are quantized actions and ν_i the respective Maslov indices [4]. The EBK tori should be determined by two quantum numbers n_1 and n_2 , whose integer values increase by one. Good candidates for these numbers are the reduced seniority \tilde{v} (connecting vertical columns of points in Fig. 7) and the radial quantum number $n_\beta = 0, 1, 2, \dots$, that enumerates states with a fixed \tilde{v} according to energy (in Fig. 7, the constant- n_β states are connected by lines). For $\eta = 0$, the radial quantum number is related to σ , which corresponds to the O(6) Casimir invariant [2], and the pair (n_β, \tilde{v}) represents the appropriate choice of the EBK quantum numbers. In the U(5)-like case, as shown below, yet an alternative pair of quantum numbers needs to be defined.

It follows from Eq. (3) that the $l = 0$ classical limit of the $\eta = 1$ Hamiltonian (1) is identical with an isotropic two-dimensional harmonic oscillator. Indeed, for the subset of states with the U(5) quantum number n_d equal to multiples of 3 (in this case $n_d = 2n_\beta + v$) the U(5) lattice coincides with the 2D-oscillator lattice of states (the energy in the latter case being enumerated by the oscillator quantum number $n_o = 2n_r + m$, where n_r and m stand for ordinary radial and angular-momentum quantum numbers, respectively). In the entire U(5) lattice, however, majority of states is located in “interstitial” positions with $n_d \neq 3k$; this is because the underlying “angular-momentum” algebra differs from the ordinary O(2). Apart from n_β and \tilde{v} , all U(5) states can be labeled by a pair of oscillator-like quantum numbers $n_1 = n_\beta + \tilde{v}$ and $n_2 = n_\beta + 2\tilde{v}$. States with constant values $n_1 = 0, 1, 2, \dots$ form upwards inclined rows of dots in Fig. 7(c), while the $n_2 = 0, 1, 2, \dots$ quantum number connects states in the downwards inclined rows. The n_1 chains are clearly apparent also in both remaining panels (a) and (b) of Fig. 7.

For the purpose of the semiclassical analysis, the lattices in Fig. 7 must be extended to cover both positive and negative π_γ . Remind from Sec. II that although the physical quantum states can be represented by non-negative values of π_γ , the intrinsic degeneracy of classical motions in both γ -directions results in mirror imaging of all states with $v > 0$ into the $\pi_\gamma < 0$ half-plane (to guarantee a smooth continuation of quantum numbers, we assign values $\tilde{v} = -1, -2, \dots$ to these “twin” states). In absence of monodromy, one must be able to engage all states in the *extended* lattice into a “crystal” grid of continuous and *smooth* lines, corresponding to constant

values of two compatible global quantum numbers, with “elementary cells” of the grid being topologically equivalent to squares. From Fig. 7(a) we see that a smooth grid, symmetric under the $\pi_\gamma \leftrightarrow -\pi_\gamma$ reflection, can be constructed in the O(6) case, using the pair of generating quantum numbers $(n_\beta, \tilde{\nu})$. In the U(5) case (panel c), this choice of quantum numbers produces a grid of lines that are broken at $\pi_\gamma = 0$, but a smooth global grid (a diagonal “chessboard”) is generated by the pair (n_1, n_2) . The latter structure can be extended to the whole interval $\eta \in [\frac{4}{5}, 1]$ where the U(5)-like spectrum exists.

In contrast, quantum monodromy implies the absence of a smooth *global* grid. This is the case of Fig. 7(b), where a smooth grid for $E < 0$ would be generated by the pair of quantum numbers $(n_\beta, \tilde{\nu})$, but for $E > 0$ by the pair (n_1, n_2) . Any attempt to define two global quantum numbers that behave smoothly in the entire lattice for $\eta \in (0, \frac{4}{5})$ fails at the point $(E, \nu) = (0, 0)$, which represents the singular torus of trajectories and, simultaneously, a “defect” in the quantum lattice of states [21, 24, 26]. It is clear that in the transition to the O(6) limit the defect is gradually pushed up to the upper edge of the lattice. For the whole interval $\eta \in (0, \frac{4}{5})$ the singular point indicates the place where the energy-momentum map passes between the O(6) and U(5) types of elementary cells—tetragons with ordered $(n_\beta, \tilde{\nu})$, $(n_\beta, \tilde{\nu} + 1)$, $(n_\beta + 1, \tilde{\nu} + 1)$, $(n_\beta + 1, \tilde{\nu})$ vertices, and analogous tetragons in (n_1, n_2) , respectively. Note that elementary cells of either type cannot be uniquely defined along a closed loop around the singular point since after one turn the cell gets distorted. This can be illustrated by a graphical construction in Fig. 7(b) and its mirror image, but the rigorous proof would require an infinite density of the lattice in the $N \rightarrow \infty$ limit. The last observation represents a common quantum signature of monodromy [21, 23, 24, 25, 26, 27, 28].

It should be stressed that monodromy in the present case is not a property of just a single Hamiltonian, but characterizes the whole $\eta \in (0, \eta_c)$ family (1) of transitional systems. Since—as shown in Part I [1]—the most substantial changes in quantum spectra of these systems take place in the $E \approx 0$ region, monodromy seems to play the key role in the process of redistribution of individual levels between the O(6) and U(5) multiplets. Related examples exist also in other parametric families of Hamiltonians, for instance, in transitions between uncoupled and coupled regimes of two quantum rotators [26] and between Zeeman and Stark limits of the hydrogen atom in crossed electric and magnetic fields [25]. Also in these examples, the crossover between the limiting spectral structures takes place at the point (or in the interval) of control parameters and energy where monodromy exists. These findings deserve further investigation.

V. CONCLUSIONS

In the present part of our work, devoted to the $[O(6)-U(5)] \supset O(5)$ transition of the interacting boson

model, we have studied the classical limit of Hamiltonian (1) with zero angular momentum. Results of the analysis of level dynamics, presented in Part I [1], were qualitatively discussed with the aid of the Berry-Tabor semiclassical trace formula, which describes fluctuations of quantum spectra in integrable systems in terms of families of periodic orbits existing at various energies. The transitional regime was exemplified by the choice of a single value of the control parameter, $\eta = 0.6$.

Both possible sources of diverging contributions to the trace formula (10), namely, the existence of bifurcating ($g_E'' = 0$) and singular ($T_{\tilde{\mu}} = \infty$) orbits, were identified in our system. While bifurcations of periodic orbits with ratios between γ - and β -vibration periods $R \in (2, 3]$ were shown to exist in the region $E > 0$, singular orbits with $\pi_\gamma = 0$ appear at $E = 0$. The latter finding led to the identification of classical monodromy, which on the quantum level exhibits itself as a defect in the lattice of quantum states located at zero values of energy and seniority. This results in the bunching of levels in the $E \approx 0$ region [1] and underlies the process of redistribution of states between O(6) and U(5) spectral structures, i.e., between the $(n_\beta, \tilde{\nu})$ and (n_1, n_2) types of elementary cells, and the respective multiplets of levels.

Also the numerical analysis of periodic and nonperiodic classical vibrations disclosed that the most substantial changes in the spectrum of allowed ratios R take place in a very narrow energy interval around $E \approx 0$. This interval represents a kind of demarcation line between the O(6) and U(5) types of classical motions. At $E \approx -0.03$, the inaccessible central disc in the plane of deformation parameters becomes sufficiently small to allow for vibrations with $R \in (2, 3]$, and at $E = 0$, when the disc vanishes, the oscillator-like orbits with $R = 2$ arise. With the energy further growing to positive values, individual vibrations with $R > 2$ eventually disappear in bifurcations (“annihilations” of two separate $\Delta\beta$ branches of a given orbit).

We believe that results of this analysis will have a concrete impact on the interpretation of data on collective vibrations in γ -soft nuclei. In a more general perspective, the $[O(6)-U(5)] \supset O(5)$ transition of the interacting boson model represents a valuable theoretical laboratory for studying structural changes between incompatible dynamical symmetries in *integrable* quantum systems.

Acknowledgments

The authors acknowledge important discussions with P. Leboeuf and Z. Pluhař. This work was supported by the DFG grant no. U36 TSE 17.2.04.

-
- [1] S. Heinze, P. Cejnar, J. Jolie, M. Macek, the preceding arXive article.
- [2] F. Iachello, A. Arima, *The Interacting Boson Model* (Cambridge University Press, Cambridge, UK, 1987).
- [3] M.C. Gutzwiller, *Chaos in Classical and Quantum Mechanics* (Springer-Verlag, New York, 1990).
- [4] H.-J. Stöckmann, *Quantum Chaos. An Introduction* (Cambridge University Press, Cambridge, UK, 1999).
- [5] M.C. Gutzwiller, J. Math. Phys. **12**, 343 (1971).
- [6] R. Balian, C. Bloch, Ann. Phys. **64**, 76 (1972).
- [7] M.V. Berry, M. Tabor, Proc. R. Soc. Lond. **A349**, 101 (1976).
- [8] B. Mottelson, Nucl. Phys. **A574**, 365c (1994).
- [9] R.L. Hatch, S. Levit, Phys. Rev. C **25**, 614 (1982).
- [10] Y. Alhassid, N. Whelan, Phys. Rev. C **43**, 2637 (1991).
- [11] N. Whelan, Y. Alhassid, Nucl. Phys. **A556**, 42 (1993).
- [12] Y. Alhassid, in *Perspectives for the Interacting Boson Model*, ed. R.F. Casten *et al.* (World Scientific, Singapore, 1994), p. 591.
- [13] A.J. Lichtenberg, M.A. Lieberman, *Regular and Stochastic Motion* (Springer-Verlag, New York, 1983).
- [14] R.H. Cushman and L. Bates, *Global Aspects of Classical Integrable Systems* (Birkhauser, Basel, 1997).
- [15] P. Cejnar, P. Stránský, Phys. Rev. Lett. **93**, 102502 (2004).
- [16] A. Klein, M. Vallieres, Phys. Rev. Lett. **46**, 586 (1981).
- [17] O. Bohigas, S. Tomsovic, D. Ullmo, Phys. Rep. **223**, 43 (1993).
- [18] G. Nicolis, *Introduction to Nonlinear Science* (Cambridge University Press, Cambridge, UK, 1995).
- [19] M. Sieber, J. Phys. A: Math. Gen. **29**, 4715 (1996); H. Schomerus, M. Sieber, *ibid.* **30**, 4537 (1997); M. Sieber, H. Schomerus, *ibid.* **31**, 165 (1998).
- [20] R.W. Robinett, Am. J. Phys. **67**, 67 (1999).
- [21] K. Efsthathiou, M. Joyeux, D.A. Sadovskii, Phys. Rev. A **69**, 032504 (2004).
- [22] J.J. Duistermaat, Commun. Pure Appl. Math. **33**, 687 (1980).
- [23] R.H. Cushman, H.R. Dullin, A. Giacobbe, D.D. Holm, M. Joyeux, P. Lynch, D.A. Sadovskii, B.I. Zhilinskiĭ, Phys. Rev. Lett. **93**, 024302 (2004).
- [24] M.S. Child, J. Phys. A: Math. Gen. **31**, 657 (1998); M.S. Child, S.H. Dong, X.G. Wang, *ibid.* **33**, 5653 (2000); S.H. Dong, Int. J. Theor. Phys. **41**, 89 (2002).
- [25] R.H. Cushman, D.A. Sadovskii, Europhys. Lett. **47**, 1 (1999); Physica D **142**, 166 (2000).
- [26] D.A. Sadovskii, B.I. Zhilinskiĭ, Phys. Lett. A **256**, 235 (1999); L. Grondin, D.A. Sadovskii, B.I. Zhilinskiĭ, Phys. Rev. A **65**, 012105 (2001).
- [27] H. Waalkens, H.R. Dullin, Ann. Phys. (N.Y.) **295**, 81 (2002).
- [28] H. Waalkens, A. Junge, H.R. Dullin, J. Phys. A: Math. Gen. **37**, L307 (2003); H. Waalkens, H.R. Dullin, P.H. Richter, Physica D **196**, 265 (2004).